



Ultra-small freestanding amorphous molybdenum sulfide colloidal nanodots for highly efficient photocatalytic hydrogen evolution reaction

Kun Chang^a, Hong Pang^{a,b}, Xiao Hai^{a,b}, Guixia Zhao^a, Huabin Zhang^a, Li Shi^{a,b}, Fumihiko Ichihara^{a,b}, Jinhua Ye^{a,b,c,d,*}

^a Photocatalytic materials group, International Center for Materials Nanoarchitectonics (WPI-MANA), National Institute for Materials Science, 1-1 Namiki, Tsukuba, Ibaraki 305-0044, Japan

^b Graduate School of Chemical Science and Engineering, Hokkaido University, Sapporo 060-0814, Japan

^c TJU-NIMS International Collaboration Laboratory, School of Materials Science and Engineering, Tianjin University, 92 Weijin Road, Tianjin, PR China

^d Collaborative Innovation Center of Chemical Science and Engineering (Tianjin), Tianjin 300072, PR China

ARTICLE INFO

Keywords:

Amorphous molybdenum sulfide
Colloidal nanodots
Ultra-small
Photocatalytic hydrogen evolution
Co-catalyst

ABSTRACT

Recently, molybdenum sulfide with its amorphous counterpart was found to hold a high activity versus the hydrogen evolution reaction (HER), making it a high potential material to explore new HER catalysts. Here we present a facile chemical method to synthesize ultra-small freestanding amorphous molybdenum sulfide (α -MoS_x) colloidal nanodots with diameter of lower than 2 nm. Electrocatalytic HER tests show that freestanding α -MoS_x colloidal nanodots exhibit an enhanced catalytic hydrogen activity in stark contrast with *in-situ* annealed c -MoS₂. When applied as a co-catalyst in photocatalytic HER, ultra-small α -MoS_x nanodots could form a compact interface with the TiO₂ when assisted by a bifunctional molecular linker, as the mercaptopropionic acid (MPA), which facilitates the decrease of the interfacial Schottky barrier occurring between the two components and allows for a fast injection of photo-excited electrons from the photoharvester into the co-catalyst. Our results demonstrate that the drastic enhancement of the photocatalytic H₂ promotion rate of α -MoS_x@MPA-TiO₂ is mainly provided by unsaturated Mo(IV) active sites generated by the *in-situ* reduction during the photocatalytic HER process. The synergistic effect of generated unsaturated Mo(IV) sites and the presence of more exposed intrinsic active edges further promotes the enhancement of the catalytic H₂ activity on α -MoS_x nanodots.

1. Introduction

The production of hydrogen fuels by using sunlight is of huge interest and could work as a sustainable solution to the global energy and environment problems [1–3]. The noble metal, Platinum (Pt) as the most efficient co-catalyst is usually loaded onto the surface of photoharvester semiconductors to produce active sites and reduce the activation energy for the surface hydrogen evolution reaction (HER) [4,5]. Serious drawbacks are related to the use of noble metals, including backward reactions during the overall water splitting, high-cost and limited-reserve in the earth. Alternative co-catalysts based on non-precious metals and metal-free materials are thus necessary to actively pursue investigations in this field [6,7]. During the past decade, significant advances have been achieved to identify HER catalysts alternative to Pt, based on transition metals such as Ni, Co, Cu, Mo, and W et al. [8–12]. In particular, crystalline molybdenum disulfide (c -MoS₂) has recently attracted a lot of attention thanks to its low cost, scalable

preparation, and attractive catalytic activities [6,13–16]. Essentially, previous studies unanimously agreed that edge planes of MoS₂ are responsible for the HER activity whereas the basal plane is inactive [11,17]. This suggested us to fabricate smaller MoS₂ crystals to create more exposed edges which could allow for a higher HER activity. However, recent studies on S-vacancies and unsaturated Mo revealed new understanding on the catalytic hydrogen mechanism of MoS₂ [18,19]. In this case, creating S-vacancies on the basal plane of MoS₂ could significantly enhance the catalytic HER activities, while the exposed unsaturated Mo exhibited much higher catalytic activities than that of edge plane. Therefore, it also provides a reasonable explanation of higher catalytic hydrogen activities for amorphous MoS_x (α -MoS_x) with disordered structure than crystalline forms [1,20], which suggests that both structural and electronic benefits for enhanced HER activity in MoS₂ have been realized by controllable disorder engineering and simultaneous oxygen incorporation. Nevertheless, exposed defects of amorphous forms simultaneously decrease the conductivity of MoS₂

* Corresponding author at: Photocatalytic materials group, International Center for Materials Nanoarchitectonics (WPI-MANA), National Institute for Materials Science, 1-1 Namiki, Tsukuba, Ibaraki 305-0044, Japan.

E-mail address: Jinhua.YE@nims.go.jp (J. Ye).

<https://doi.org/10.1016/j.apcatb.2018.03.087>

Received 16 January 2018; Received in revised form 22 March 2018; Accepted 25 March 2018

Available online 26 March 2018

0926-3373/ © 2018 Elsevier B.V. All rights reserved.

itself, which extremely restricts the electron mobility and decrease its catalytic activity. To make quantum sized and freestanding MoS_x nanodots is expected to be the most effective way to improve the catalytic activity versus HER, only providing more active sites but also to achieve a good dispersion on the surface of electrode supporters or photoharvester semiconductors, by facilitating the charge transfer kinetics.

In this work, we first describe a facile chemical synthesis method to successfully prepare the colloidal $\alpha\text{-MoS}_x$ nanodots with the diameter of lower than 2 nm. After complexing with mercaptopropionic acid (MPA) ligands, a stable and monodispersed colloidal solution was obtained. The HER tests show that the proposed freestanding $\alpha\text{-MoS}_x$ colloidal nanodots exhibit an enhanced catalytic hydrogen activity in stark contrast with the $c\text{-MoS}_2$ which are *in-situ* annealed at high temperature. Likewise, when the co-catalyst is deposited on a metal oxide semiconductor such as TiO_2 , $\alpha\text{-MoS}_x\text{@MPA}$ colloidal nanodots showed a uniform and compact adsorption on the photoharvester surface, delivering an excellent photocatalytic activity. Although the ultra-small structure of $\alpha\text{-MoS}_x$ on the TiO_2 surface caused a partial oxidation of Mo atoms, it could be further reduced into unsaturated Mo(IV) active sites with high catalytic activity during the photocatalytic HER, facilitating the subsequently drastic enhancement of H_2 promotion.

2. Experimental details

General: All chemical reagents were supplied by Wako and Sigma-Aldrich and were used without further purification.

2.1. Synthesis of $\alpha\text{-MoS}_x$ colloidal nanoparticles

First, 2 mmol Li_2CO_3 (99.9%, Wako) were dissolved into 5 ml deionized (DI) water. Then, 2 mmol $(\text{NH}_4)_2\text{MoS}_4$ (99.97%, Aldrich) were added to the solution. The solution was then transferred into an alumina crucible which was placed at the center of the furnace tube. Under the protection of Ar atmosphere, the temperature was first raised to 353 K and kept for 12 h to eliminate water in the precursors. Subsequently, the temperature was increased to 1073 K with 4 h, kept for 4 h and then allowed to cool down to room temperature naturally. Annealed samples were then added into deoxygenized DI water by Ar gas with stirring after being sonicated for several minutes. Filtration was applied to remove residuals and the obtained colorless solution was titrated by 0.5 M HCl solution to control the pH value. With the injection of HCl solution, a red brown sediment immediately appeared. Excessive HCl resulted in a complete sedimentation of bulk $\alpha\text{-MoS}_x$, which could be used to calculate the MoS_2 content in the solution.

2.2. Synthesis of free standing $\alpha\text{-MoS}_x\text{@MPA}$ colloidal nanodots

Similarly with the above procedure, a certain amount of MPA solution was added into the solution titrated into a pH around 6, and then the HCl excess was added. As-synthesized $\alpha\text{-MoS}_x\text{@MPA}$ colloidal solution was kept to 277 K for later use.

2.3. Preparation of electrodes for electrochemical test

For FTO supported $\alpha\text{-MoS}_x\text{@MPA}$ colloidal nanodots FTO was cleaned in ethanol and acetone and then immersed into the as-prepared $\alpha\text{-MoS}_x\text{@MPA}$ colloidal solution for seconds, then washed with deoxygenized DI water and dried under Ar flow. FTO supported $c\text{-MoS}_2$ was prepared *in-situ* by the calcination at 673 K for 4 h under Ar atmosphere. TiO_2 nanoparticles were deposited on FTO by spin-coating and then calcined at 673 K for 4 h in air.

2.4. Preparation of the $\alpha\text{-MoS}_x\text{@MPA-TiO}_2$ and $c\text{-MoS}_2/\text{TiO}_2$ nanocomposites

0.5 g commercial P25- TiO_2 powders (Wako) were dispersed in

200 mL deoxygenized DI water. A certain amount of $\alpha\text{-MoS}_x\text{@MPA}$ colloidal solution was added and stirred. Products were then quickly washed with deoxygenized DI water through vacuum filtering and then transferred into vacuum drying oven at 323 K. The $c\text{-MoS}_2/\text{TiO}_2$ nanocomposite was obtained by the *in-situ* calcination of as-prepared $\alpha\text{-MoS}_x\text{@MPA-TiO}_2$ samples at 673 K for 4 h under Ar atmosphere.

2.5. Characterizations

The samples were characterized by X-ray diffraction (XRD, RINT-2000; Rigaku Corp., Japan) with $\text{Cu K}\alpha_1$ radiation, atomic force mode (AFM, Nanoscope H, Japan), and Raman spectra (Horiba-Jobin-Yvon, T64000, Japan). TEM images, combined with energy-dispersive X-ray spectroscopy (EDS) mapping were recorded with a field emission transmission electron microscope (JEM2100F, JEOL Co., Japan) operating at 200 kV. UV-vis diffuse reflectance spectra were measured using the diffuse reflection method with a Shimadzu UV-2500 spectrophotometer. XPS data were collected using a PHI Quantera SXM (ULVAC-PHI, Japan). EPR spectra were recorded on a JES-FA200 electron spin resonance spectrometer operating at about 9.0 GHz at room temperature.

2.6. Electrochemical measurements

Electrochemical measurements were performed in a standard three-electrode system using a CHIALS/CH-660 instrument. A graphite rod, Ag/AgCl (saturated KCl), and a FTO electrode were used as counter, reference, and working electrodes, respectively. All the measurements were performed in 0.5 M H_2SO_4 aqueous solution under continuous purging with Ar at room temperature, with a sweep rate of 5 mV s^{-1} . Cyclic voltammograms at various scan rates (20, 40, 60, 80, 100, 120, 140, 160, 180, and 200 mV/s) were collected in the 0.1–0.2 V vs RHE range and used to estimate the double-layer capacitance. The electrochemical impedance spectroscopy (EIS) measurements were carried out at 200 mV overpotential with the frequency ranging from 10^6 to 0.1 Hz.

2.7. Photocatalytic H_2 evolution

The photocatalytic H_2 evolution was carried out with 100 mg photocatalyst suspending in 300 mL solution in a Pyrex glass reaction cell. The reaction cell was connected to a gas-closed system with a gas-circulated pump. Ultraviolet light was produced by a 300 W Xe lamp ($\lambda > 300 \text{ nm}$). The evolved H_2 was analyzed using an on-line gas chromatograph (GC-8A, Shimadzu Co., Japan) equipped with a thermal conductivity detector (TCD.) The apparent quantum efficiency (AQE) was measured by applying a Xe lamp (300 W) with a 367 (± 20) nm band-pass filter (MIF-W, Optical Coatings Japan Co., Japan). The number of incident photons was measured using a radiant power energy meter (Ushio Spectroradiometer, USR-40).

3. Results and discussion

3.1. Characterization of $\alpha\text{-MoS}_x$ colloidal nanodots

The process for the formation of $\alpha\text{-MoS}_x$ colloidal nanodots is illustrated in Fig. 1a. It is known that during the traditional thermal decomposition of $(\text{NH}_4)_2\text{MoS}_4$, the first step involves the decomposition to form MoS_3 and the release of NH_3 and H_2S gas. The second step is then the decomposition of the MoS_3 to form MoS_2 [21]. Given this, to prevent the aggregation and crystallization of the final MoS_2 , in our designed experiment ammonium ions in $(\text{NH}_4)_2\text{MoS}_4$ were replaced by lithium ions to form Li_2MoS_4 . After calcination, nonvolatile Li_2S was *in-situ* kept in proximity of MoS_2 (Fig. S1a). In the subsequent step, part of Li_2MoS_3 ($\text{Li}_2\text{S} + \text{MoS}_2$) was dissolved in water and to form an alkaline transparent solution (Fig. S1b). We propose that this might be caused by the reaction of Li_2MoS_3 complex with HCl and followed by the

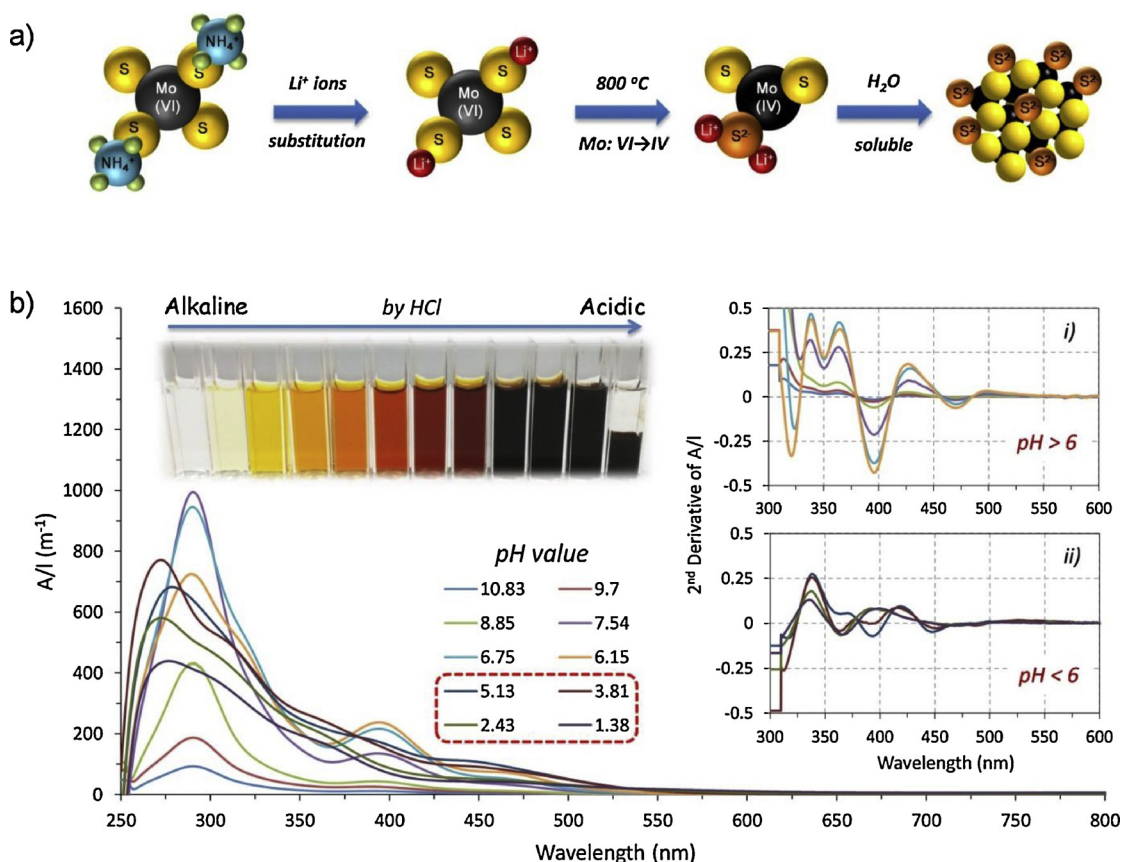


Fig. 1. (a) Schematic illustration of growth process of α - MoS_x colloidal nanodots. (b) UV-vis absorption spectra of α - MoS_x colloidal nanodots synthesized at different pH-values; the inset shows the color change with the pH value, (i) and (ii) clearly show the absorption peaks by the second derivative of the spectra.

formation of a soluble $n[\text{MoS}_x]\text{S}^{2-}$ complex (Fig. 1a). Excessive HCl results in $n[\text{MoS}_x]\text{S}^{2-}$ complexes losing the S^{2-} protection and finally aggregating (Fig. S2). To confirm this speculation, UV-vis absorption spectra were performed to detect the characteristics of each suspension solution at different pH values by adjusting the HCl, as shown in Fig. 1b. With the decrease of the pH value, two exciton peaks located at 470 nm (λ_{470}) and 395 nm (λ_{395}) appear which are assigned to soluble $n[\text{MoS}_x]\text{S}^{2-}$ complex [19]; this was associated with color change in the solution (see insert in Fig. 1b). The second derivative of the absorption spectra (Fig. 1bi and bii) shows the variation of λ_{470} and λ_{395} peaks more clearly. When the solution system is neutral or alkaline, i.e., $\text{pH} > 6$, the intensities of λ_{470} and λ_{395} peaks reach their maximum. However, when pH value was lower than 6, both extinction peaks almost disappeared, simultaneously accompanied with the formation of a red brown precipitate; the presence of only two broad X-ray diffraction peaks, as shown in Fig. S3a, suggests the formation of an amorphous compound. After the heat treatment, significant diffraction peaks appeared and were assigned to the 2H-type c - MoS_2 .

Fig. 2a (red trace) shows the resonance Raman spectrum of an as-prepared amorphous precipitate. Remarkably, two prominent peaks corresponding to the in-plane E_{2g}^1 and out-of-plane A_{1g} modes of MoS_2 can be clearly seen in the amorphous precipitate which have identical Raman signatures respect to those of c - MoS_2 rather than the reported $[\text{Mo}_3\text{S}_{13}]^{2-}$ clusters [22]. In addition, the broad weak peak in the range between 700 and 1000 cm^{-1} was assigned to $\text{Mo}=\text{O}$ or $\text{Mo}(=\text{O})_2$ vibration band indicating the presence of unsaturated Mo exposed in such as-synthesized disordered α - MoS_x precipitate.[19] Similar signatures were also obtained for α - MoS_x precipitate and annealed bulk c - MoS_2 using X-ray photoelectron spectroscopy (XPS, Figs. 2b, c, and S3). Based on the analysis of the Mo 3d spectrum, the $3d_{3/2}$ peak at 232.2 eV and $3d_{5/2}$ peak at 229.7 eV, indicate the characteristic +4 oxidation state,

[23] while the doublet at 234.1 and 231.1 eV correspond to the Mo (V) oxidation state.[24] For both as-prepared and annealed samples, the deconvolution of the Mo 3d peaks revealed a Mo^{6+} 3d signal at around 236.1 eV, likely due to the slight surface oxidation upon exposure to air [25]. In the S 2p core-level spectra, the c - MoS_2 has only a single doublet observed at 163.6 and 162.5 eV corresponding to S $2p_{1/2}$ and S $2p_{3/2}$ orbitals, while the α - MoS_2 exhibits an additional doublet at 165.1 and 163.8 eV, which was identified to the disordered S [25,26]. These results indicate that the amorphous and noncrystalline MoS_x presents numerous disordered S and S-vacancies which can be successfully synthesized through the proposed chemical method.

3.2. Application of α - MoS_x colloidal nanodots in electro-catalytic HER

To prevent the aggregation of α - MoS_x bulk particles, MPA was used to complex the $n[\text{MoS}_x]\text{S}^{2-}$ colloidal nanodots at the $\text{pH} \approx 6$ to form a red soluble α - MoS_x @MPA colloidal solution (Fig. 3a). The thiolate group in MPA showed a good affinity with exposed Mo from α - MoS_x nanocrystal, and therefore the α - MoS_x @MPA complex can steadily exist in the acidic solution (Fig. S4). Due to the effective binding of carboxylate group to metal oxides, the bifunctional molecular linker MPA is used to assist the assembly of metal sulfides with metal oxides [27,28]. Given this, Atomic Force Microscope (AFM) characterization was performed on a piece of mica which was immersed in the α - MoS_x @MPA colloidal solution and then washed by the distilled water to remove impurities. Results show that the average height of the partial adsorbed α - MoS_x @MPA nanodots is less than 1.5 nm (Figs. 3b–d and S5). Likewise, α - MoS_x @MPA colloidal nanodots were adsorbed by self-assembly on the surface of fluorine-doped tin oxide (FTO) for the electrochemical HER tests (Fig. 3e). The catalytic hydrogen activity of the α - MoS_x @MPA colloidal nanodots was evaluated using a three-

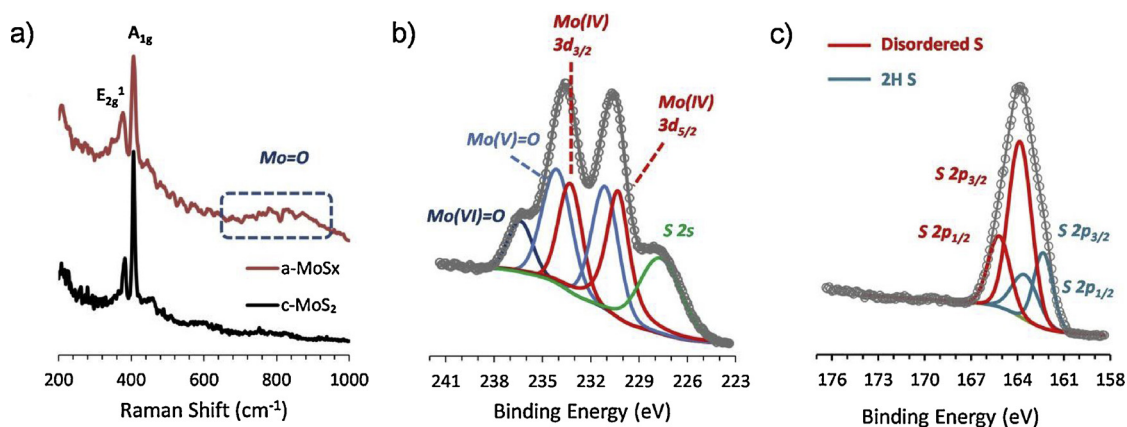


Fig. 2. (a) Resonance Raman spectra (532 nm laser excitation) of the α -MoS_x bulk precipitate and c -MoS₂ after annealing at 400 °C in Ar atmosphere. (b, c) XPS core-level spectra and deconvolution into Mo 3d and S 2p contributions for a freshly as-synthesized α -MoS_x bulk precipitate.

electrode electrochemical cell. Fig. 2f shows linear-sweep voltammograms (LSV) in the cathodic direction for the bare blank FTO compared to that with α -MoS_x@MPA colloidal nanodots, and *in-situ* formed c -MoS₂. The blank FTO surface shows no HER activity in the investigated potential window, only a weak reduction peak at around -0.4 V versus reversible hydrogen electrode (RHE), which is assigned to the reduction of Sn⁴⁺ in FTO. In contrast with c -MoS₂, the α -MoS_x@MPA colloidal nanodots on FTO electrode show a sharp exponential increase in the

magnitude of the cathodic current density with the increase of the overpotential, indicating a high HER activity. A reduction peak at ~ 0.08 V appeared in the first LSV scan of α -MoS_x@MPA nanodots (insert in Fig. 3f), while it was not seen in the subsequent polarization curves. This factor was attributed to the removal of S or O atoms bonding with Mo (V or VI) to generate unsaturated catalytic Mo (IV) centers for H₂ evolution [19,29]. The corresponding Tafel plots from the logarithm of the current density versus the overpotential are shown

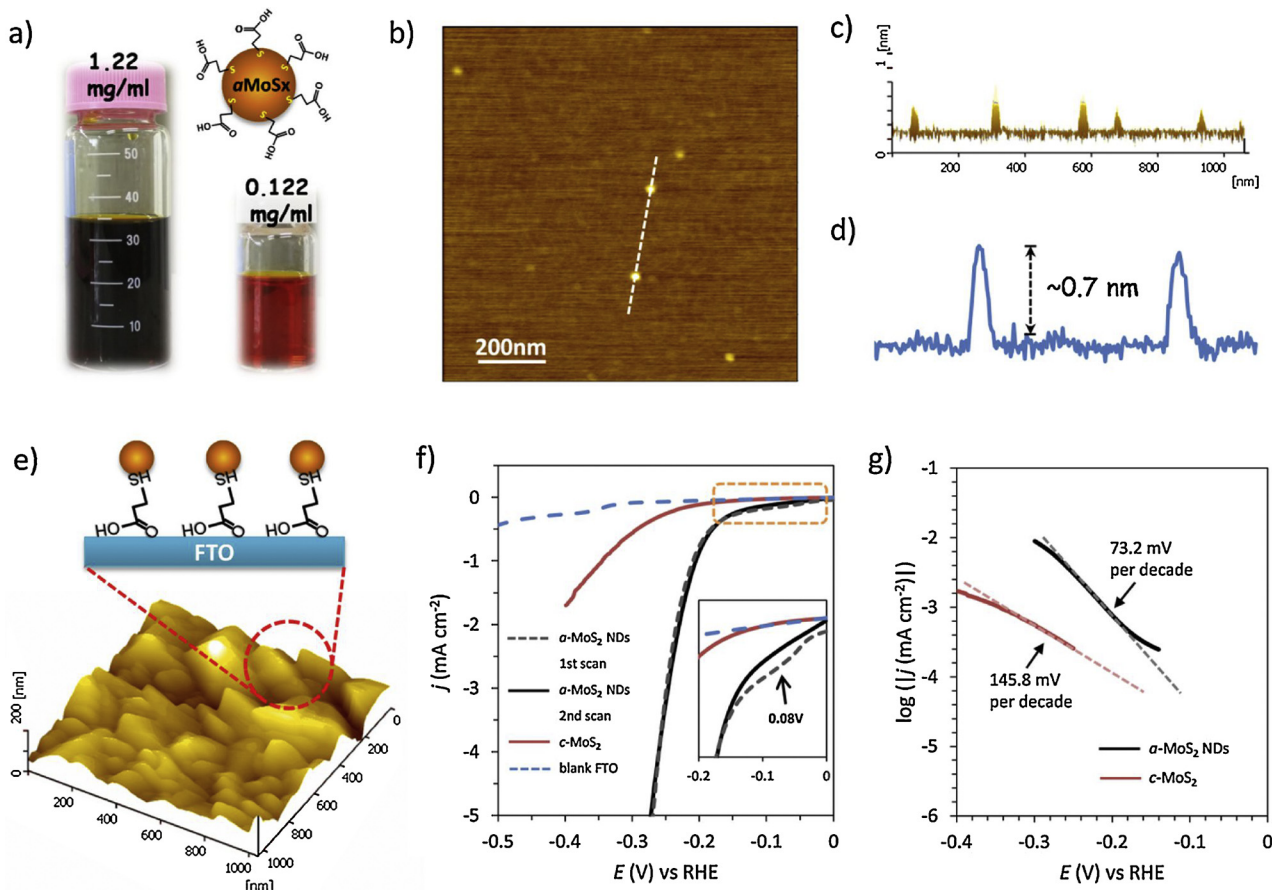


Fig. 3. Analysis of freestanding α -MoS_x@MPA colloidal nanodots and their catalytic H₂ evolution activity. (a) Photograph of colloidal nanodot solution. (b–d) AFM analysis of nanodots deposited on mica, (c) cross-section 3D mode of AFM image, and (d) height profile along the dashed line in (b). (e) 3D mode AFM image of FTO supported α -MoS_x@MPA nanodots. (f, g) electrochemical characterization of α -MoS_x@MPA nanodots and *in-situ* formed c -MoS₂ electrode for HER; (f) J -V curves of various electrodes in 0.5 M H₂SO₄ aqueous solution. The inset shows the enlarged selected region of comparison of first two LSV scans of α -MoS_x@MPA film; (g) corresponding Tafel plots for the data presented in (f). (For interpretation of the references to colour in the text, the reader is referred to the web version of this article.)

in Fig. 3g. The 73.2 mV per decade of Tafel slope for α -MoS_x@MPA is not only lower than that of *in-situ* annealed *c*-MoS₂, but also lower than that of bulk ones (Fig. S6). Furthermore, the double-layer capacitances (C_{dl}) derived from the cyclic voltammogrammetry measurement (Fig. S7), which is proportional to the efficient electrochemically active surface area, is measured to evaluate the effective surface area before and after the crystallization of α -MoS_x@MPA samples. Remarkably, the as-prepared α -MoS_x@MPA nanodots present more catalytically active sites respect to *in-situ* formed *c*-MoS₂, in agreement with the HER activity. Electrochemical impedance spectroscopy (EIS) was further performed to investigate the electrode kinetics during the HER process. Nyquist plots (Fig. S7d) were fitted using an equivalent circuit (inset of Fig. S7d) to extract the charge transfer resistance (R_{ct}) of 68.3 and 362.1 Ω for α -MoS_x@MPA and *c*-MoS₂ at -0.2 V versus RHE. The significant decrease of the R_{ct} of the α -MoS_x@MPA suggests a fast Faradaic process and thus superior HER kinetic in contrast to *in-situ* formed *c*-MoS₂. It is noteworthy that although the current density and active surface area of proposed α -MoS_x@MPA electrode is lower than that of recent reports [30–33], which is mainly due to the lower quantity of α -MoS_x@MPA nanodots adsorption (Fig. S7e), these results provides a stark comparison between the catalytic H₂ activity of α -MoS_x and *c*-MoS₂ under comparable conditions, which has a significance for guiding further application as a co-catalyst in photocatalytic HER.

3.3. Application of α -MoS_x colloidal nanodots in photo-catalytic HER

In most cases of photocatalytic HER, co-catalysts are loaded for promotion of H₂ evolution, presumably because most photocatalysts do not offer an active site for catalytic H₂ evolution on the surface [6]. The co-catalysts are usually required to have the particle size ranging from 1 to 10 nm, which loaded onto the photocatalyst surface as a dispersion of nanoparticles to produce active sites and reduce the activation energy for surface chemical reactions [34]. However, for the most of MoS₂-based co-catalysts with typical two-dimensional layered structure, it is difficult to effectively form a compact interface with the photoharvester semiconductors, like TiO₂, most representatively, where the high interfacial Schottky barrier hinders the injection of photo-excited electrons from the photoharvesters into the co-catalysts. Our proposed freestanding α -MoS_x@MPA colloidal nanodots could effectively solve this critical issue. When mixed with the commercial TiO₂ (P25, particle size less than 50 nm) in aqueous solution, α -MoS_x@MPA nanodots immediately adsorb on the TiO₂ surface due to the strong binding between carboxylate group of MPA and Ti from TiO₂ (Fig. 4a and c). TEM images (Fig. 4d and e) and the elemental mapping (Fig. S8) show α -MoS_x@MPA nanodots with an average diameter of 1–2 nm uniformly dispersed on TiO₂ nanoparticles. Meanwhile, to better illustrate the catalytic hydrogen activity of α -MoS_x nanodots, results were compared with *c*-MoS₂ *in-situ* synthesized on the surface of TiO₂ from the heat treatment of α -MoS_x@MPA/P25 in Ar atmosphere (Fig. 4a). Fig. 4b compares the UV–vis diffuse reflectance spectra of P25-TiO₂, α -MoS_x@MPA/P25, and *c*-MoS₂/P25, respectively. Two distinct additional peaks located at 650 nm (A-exciton) and 600 nm (B-exciton) from *c*-MoS₂/P25 were assigned to the direct excitonic transitions of *c*-MoS₂ at the K point of Brillouin zone [35,36]. This implies that the amorphous MoS₂ was transferred into its semiconducting crystalline form. In addition, λ_A with only 650 nm corresponding to the band gap of ~ 1.9 eV indicates a result of quantum-confinement effect which was previously proposed for *c*-MoS₂. [37] The introduction of MPA affected the red-shift of UV–vis absorption because of the carboxyl group adsorption which has a strong interaction with TiO₂ surface (Fig. S9), broadening its photoharvesting range [38]. Fig. 4f shows that *c*-MoS₂ particles with the interlayer spacing of 0.62 nm are uniformly formed on the TiO₂ surface. The presence of defective Mo(V)=O sites within α -MoS_x@MPA nanodots loaded on the surface of TiO₂ was evidenced by XPS analysis on Mo 3d orbitals, as shown in Fig. 4g. Compared with the bulk α -MoS_x (Fig. 2b), the proportion of Mo with a + 5 oxidation state in α -MoS_x

nanodots was increased, presumably because of the more susceptible oxidation of small nanostructures when exposed to air. After the heat treatment, Mo with high oxidation states is transferred into the typical crystalline form with a + 4 oxidation state (Fig. 4h); the absence of Mo=O bonds is likely due to the thermal reduction by thiolate groups from MPA.

Photocatalytic H₂ evolution tests were carried out with 100 mg of the photocatalyst hybrids in 300 mL of methanol aqueous solution (20 vol.%) in a Pyrex glass reaction cell. A 300 W xenon lamp was used as the light driven source. Fig. 5a shows the dependence of the photocatalytic activity from the loading amount of α -MoS_x@MPA colloidal nanodots over TiO₂. It is seen that the rate of H₂ evolution increases with the increase of the α -MoS_x@MPA-loading from 0 to 1.5 wt.%. When the loading amount of α -MoS_x@MPA is increased to 1.5 wt.%, the catalytic activity reaches the maximum, value of 259.2 $\mu\text{mol h}^{-1}$ with an apparent quantum efficiency (AQE) of 14.9% at 367 (± 20) nm (Fig. S10). It is worth noting that this is inconsistent with previous reports where the loading amount of co-catalyst is usually controlled at less than 3 wt.% and the presence of excessive dark-color co-catalysts on the surface of semiconductor blocks the light transmission and further decreases the catalytic H₂ activity [39,40], our proposed α -MoS_x@MPA-TiO₂ photocatalyst hybrids keep a high catalytic activity even at a high co-catalyst loading (Fig. 5a). This fact was attributed to the ultra-small structure of the α -MoS_x@MPA colloidal nanodots. After excluding the self-decomposition of methanol under the UV light irradiation (Fig. S11), Fig. 5b and c show the comparison between the bare TiO₂, α -MoS_x@MPA-TiO₂ (1.5 wt.%), and *in-situ* formed *c*-MoS₂/TiO₂. Bare P25-TiO₂ does not provide active sites for catalytic hydrogen evolution on the surface due to its high crystallinity, leading to the facile recombination of photo-excited electron-hole pairs before their migration to the surface where reactions can occur [4]. Therefore the bare P25-TiO₂ was inactive versus the catalytic hydrogen evolution (0.3 $\mu\text{mol h}^{-1}$). Although nanosized MoS₂ with 2H crystalline phase was reported as a high potential electrocatalysts and co-catalysts in HER [41–43], there is no obvious activity improvement in our *c*-MoS₂/TiO₂ hybrid photocatalyst (only 32.5 $\mu\text{mol h}^{-1}$). However, the α -MoS_x@MPA-TiO₂ nanocomposite exhibits a drastic enhancement in the photocatalytic hydrogen evolution activity reaching eight times higher value respect to *c*-MoS₂/TiO₂. We also measured the photocatalytic H₂ activity of MPA/TiO₂ sample in Fig. S11. After 9-h UV light irradiation, 5.3 μmol of H₂ amount was detected, with $\sim 0.6 \mu\text{mol h}^{-1}$ of H₂ production rate. Compared with α -MoS_x@MPA-TiO₂ catalyst with 259.2 $\mu\text{mol h}^{-1}$ of H₂ generation rate, the MPA didn't play the decisive effect of H₂ evolution activity. This indicates that amorphous MoS₂ possess a higher HER activity respect to crystalline forms. This was ascribed to two aspects: one is in agreement with a previous study [44], showing that crystalline 2H-MoS₂ presents semiconducting properties with a direct band gap of ~ 1.9 eV. Electronic energy levels are thus mismatched with TiO₂, i.e., the conduction band (CB) of *c*-MoS₂ is equal or more negative than that of TiO₂, resulting in a sluggish charge transfer from the TiO₂CB to the CB of MoS₂ (Fig. S12); the second factor is ascribed to the presence of unsaturated Mo(IV) sites within α -MoS_x nanodots. We noticed that during the photocatalytic H₂ evolution tests on α -MoS_x@MPA-TiO₂ samples (Figs. 5b and S13), the H₂ production was not linearly increasing with the irradiation time, although this was the case in the two other samples. The high catalytic H₂ evolution activity of the α -MoS_x@MPA-TiO₂ photocatalysts usually requires a certain irradiation time to be activated, this time results to depend on α -MoS_x@MPA co-catalyst loading. This process was attributed to the reduction of Mo(V)=O bonds within the nanodots which creates catalytically active unsaturated Mo(IV) sites; Mo-bound hydride species act as the highly-active species in the photocatalytic HER [17,19].

To validate this hypothesis, the XPS Mo 3d spectrum of α -MoS_x@MPA-TiO₂ nanocomposite was measured after the photocatalytic HER (Fig. 5d) by carefully avoiding air exposition. Compared with the as-prepared α -MoS_x@MPA-TiO₂ sample, the proportion of Mo 3d doublet

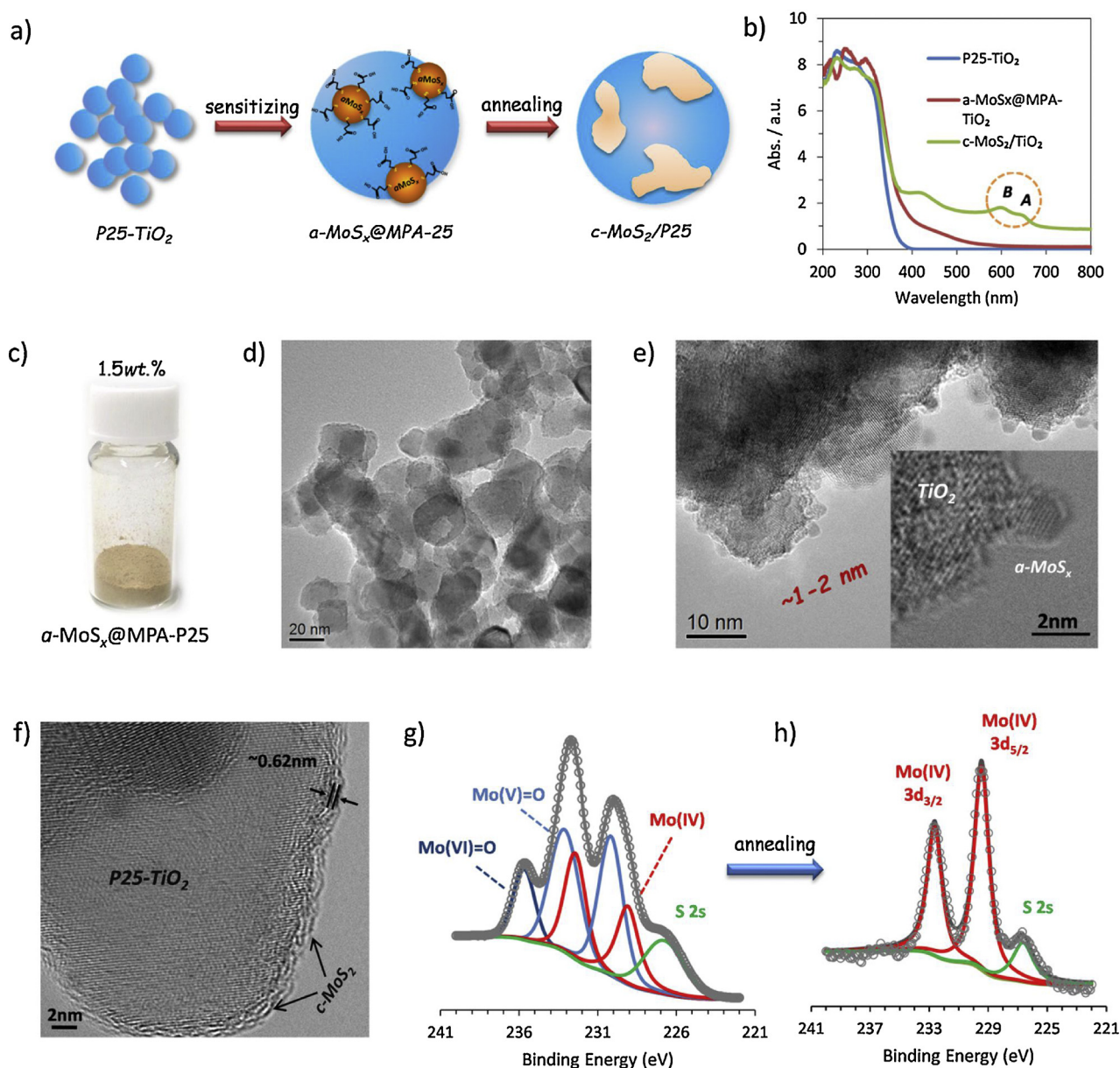


Fig. 4. Characterization of different MoS₂ on TiO₂ photocatalysts. (a) Schematic illustration of the process for growing α-MoS_x@MPA nanodots and c-MoS₂ on the surface of TiO₂. (b) Corresponding UV-vis absorption spectra. (c) Photograph of the α-MoS_x@MPA-TiO₂ photocatalyst with a co-catalyst loading of 1.5 wt.%. (d, e) TEM images of uniformly dispersed α-MoS_x@MPA nanodots on TiO₂, showing the ultra-small structure. (f) TEM observation of *in-situ* formed c-MoS₂ on TiO₂. (g, h) XPS core-level spectra and deconvolution into Mo 3d contributions for α-MoS_x@MPA-TiO₂ and c-MoS₂/TiO₂.

with + 5 oxidation state significantly decreased, indicating a strong reduction of the Mo(V). Combining this result with the increase of the H₂ production rate with the irradiation time, it is reasonably to assign to the *in-situ* generated unsaturated catalytical Mo(IV) sites for the enhanced HER. In addition, electron paramagnetic resonance (EPR) spectroscopy to provide information for a paramagnetic signal of the generated active centers in Fig. S14. It can be seen that TiO₂ and α-MoS_x@MPA/TiO₂ do not show any paramagnetic signals except for Mn standard peaks. However, after UV light irradiation in methanol aqueous solution, α-MoS_x@MPA/TiO₂ sample shows an obvious signal at ~321 mT with g factor of 2.003. Generally, the signal in the range of g value from 1.91 to 2.003 in MoS₂ compound can be ascribed to the contribution from Mo–S dangling bonds and S-vacancies [45,46]. This phenomenon also implies that Mo (V)=O centers caused by S-vacancies could be reduced into unsaturated Mo (IV) centers by photo-excited electrons from TiO₂. In conclusion ultra-small α-MoS_x colloidal nanodots possess numerous exposed active edges which promote the HER

rate (Fig. 5e). Moreover, due to the ultra-small particle size and the amorphous state, the partially disordered S atoms are easily substituted by O to form Mo(V)=O centers, which can be further reduced into unsaturated Mo(IV) sites which are active sites during the photocatalytic HER, and promote the H₂ production. The α-MoS_x@MPA-TiO₂ nanocomposite also exhibits a high stability and no noticeable loss of activity for photocatalytic H₂ production after five cycles (Fig. 5f). Table S1 compares the HER activity of recently reported MoS₂-TiO₂ photocatalysts, showing that the α-MoS_x@MPA-TiO₂ nanocomposite delivers the highest photocatalytic H₂ activity. This mainly depends on the close contact between ultra-small α-MoS_x@MPA nanodots and TiO₂, which decreases the interfacial Schottky barrier and facilitates the transport of photo-generated electrons.

4. Conclusions

In summary, we described a facile and novel chemical synthesis

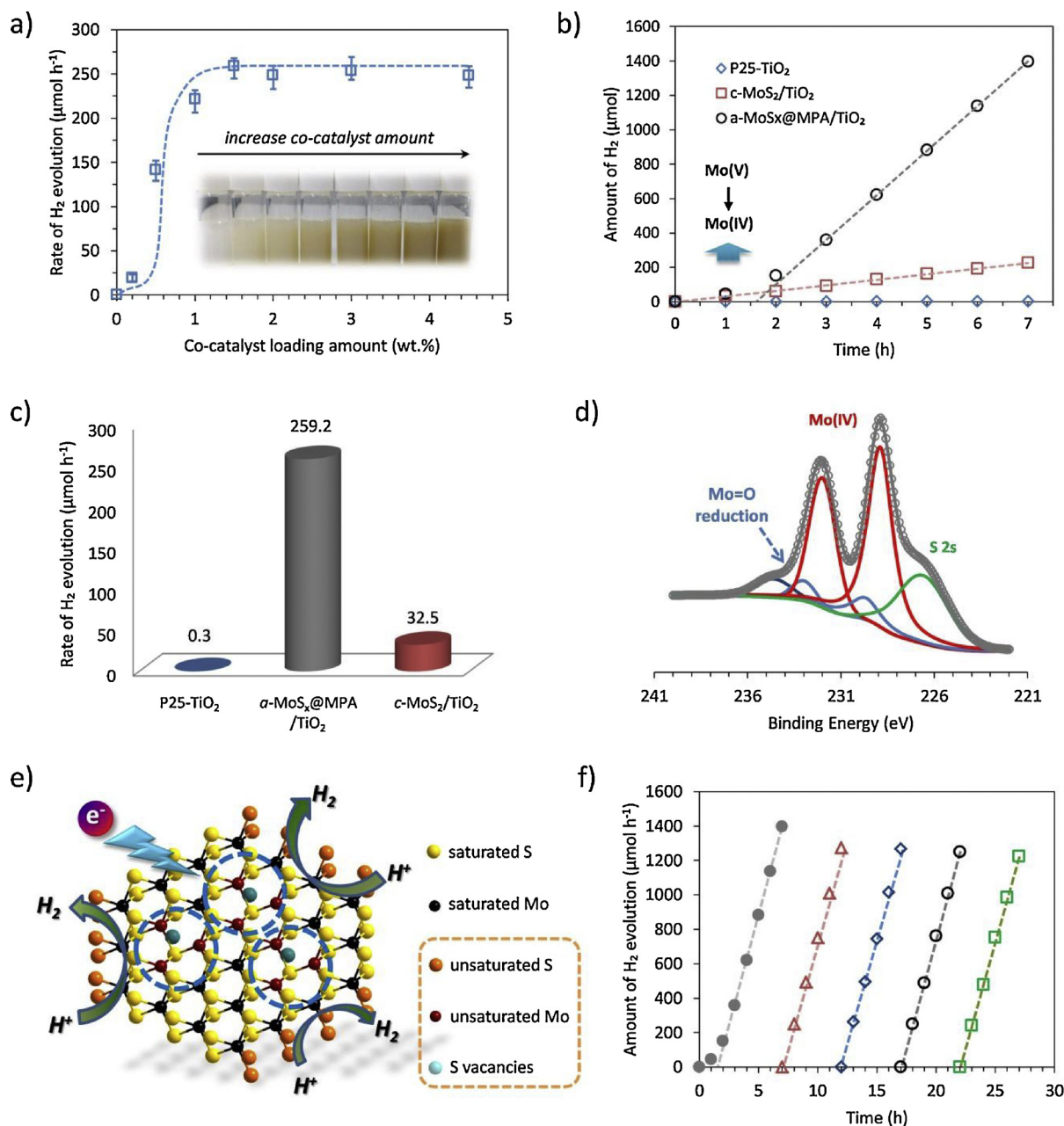


Fig. 5. Evaluation of photocatalytic H₂ activity of various MoS₂ forms loaded on TiO₂. (a) Dependence of the photocatalytic H₂ evolution rate from the α-MoS_x@MPA-TiO₂ catalyst loading; the inset shows the change of the solution color with the loading amount. (b, c) Comparison between the activity for the bare TiO₂, c-MoS₂/TiO₂ and α-MoS_x@MPA-TiO₂ catalysts. (d) XPS core-level spectral analysis on Mo 3d orbital from the α-MoS_x@MPA-TiO₂ after the photocatalytic HER test. (e) Illustration of the proposed catalytically active sites for H₂ evolution within the α-MoS_x nanodots. (f) Cycling test revealing the stability of the α-MoS_x@MPA-TiO₂ photocatalyst during five HER cycles. Light source: 300 W Xe lamp, λ > 300 nm; Reaction solution: 300 mL methanol aqueous solution (20%); Cat. 100 mg.

method to successfully prepare stable and monodispersed colloidal α-MoS_x@MPA nanodots with the diameter of lower than 2 nm. Assisted by a bifunctional molecular linker MPA, the monodispersed α-MoS_x nanodots were assembled on a metal oxide. Electrochemical HER tests showed that the TiO₂ supported α-MoS_x@MPA nanodots exhibited higher integrated catalytic H₂ activity respect to *in-situ* formed c-MoS₂, including a lower overpotential, a smaller Tafel slope, a larger double-layer capacitance and a smaller charge-transfer resistance. During the photocatalytic HER experiments, freestanding α-MoS_x@MPA colloidal nanodots could effectively form a compact interface with the TiO₂, facilitating the decrease of interfacial Schottky barrier between the two components and the fast injection of photo-excited electrons from the photoharvester into the co-catalysts. Although ultra-small α-MoS_x nanodots on the TiO₂ surface caused a certain oxidation state of Mo

atoms, photocatalytic HER process could provide their reduction into unsaturated Mo(IV) sites providing for a high photocatalytic activity versus HER and facilitating the enhancement of H₂ production. This study presents new and comprehensive insights which reveal the critical factors that affect the catalytic performances of α-MoS_x, particularly relevant in the field of photocatalytic HER for MoS₂-metal oxide systems.

Acknowledgments

This work received financial support from the World Premier International Research Center Initiative (WPI Initiative) on Materials Nano-architectonics (MANA), MEXT (Japan), the National Basic Research Program of China (973 Program, 2014CB239301), the

National Natural Science Foundation of China (21633004), and the JSPS KAKENHI (Grant No. 16F16049). We also appreciated Dr. Toshiaki Takei in MANA, NIMS providing TEM and EDS characterizations support.

Appendix A. Supplementary data

Supplementary material related to this article can be found, in the online version, at doi:<https://doi.org/10.1016/j.apcatb.2018.03.087>.

References

- J.F. Xie, J.J. Zhang, S. Li, F. Grote, X.D. Zhang, H. Zhang, R.X. Wang, Y. Lei, B.C. Pan, Y. Xie, Controllable disorder engineering in oxygen-incorporated MoS₂ ultrathin nanosheets for efficient hydrogen evolution, *J. Am. Chem. Soc.* 135 (2013) 17881–17888.
- H. Tong, S.X. Ouyang, Y.P. Bi, N. Umezawa, M. Oshikiri, J.H. Ye, Nano-photocatalytic materials: possibilities and challenges, *Adv. Mater.* 24 (2012) 229–251.
- J.A. Turner, Sustainable hydrogen production, *Science* 305 (2004) 972–974.
- J. Ran, J. Zhang, J. Yu, M. Jaroniec, S.Z. Qiao, Earth-abundant cocatalysts for semiconductor-based photocatalytic water splitting, *Chem. Soc. Rev.* 43 (2014) 7787–7812.
- Z.W. Seh, J. Kibsgaard, C.F. Dickens, I. Chorkendorff, J.K. Nørskov, T.F. Jaramillo, Combining theory and experiment in electrocatalysis: insights into materials design, *Science* 355 (2017) eaad4998.
- K. Chang, X. Hai, J.H. Ye, Transition metal disulfides as noble-metal-alternative Cocatalysts for solar hydrogen production, *Adv. Energy Mater.* 6 (2016) 1502555.
- X.X. Zou, Y. Zhang, Noble metal-free hydrogen evolution catalysts for water splitting, *Chem. Soc. Rev.* 44 (2015) 5148–5180.
- A. Le Goff, V. Artero, B. Jusselme, P.D. Tran, N. Guillet, R. Metaye, A. Fihri, S. Palacin, M. Fontecave, From hydrogenases to noble metal-free catalytic nanomaterials for H₂ production and uptake, *Science* 326 (2009) 1384–1387.
- E.S. Andreiadis, P.A. Jacques, P.D. Tran, A. Leyris, M. Chavarot-Kerlidou, B. Jusselme, M. Matheron, J. Pecaut, S. Palacin, M. Fontecave, V. Artero, Molecular engineering of a cobalt-based electrocatalytic nanomaterial for H₂ evolution under fully aqueous conditions, *Nat. Chem.* 5 (2013) 48–53.
- J.R. McKone, S.C. Marinescu, B.S. Brunshwig, J.R. Winkler, H.B. Gray, Earth-abundant hydrogen evolution electrocatalysts, *Chem. Sci.* 5 (2014) 865–878.
- T.F. Jaramillo, K.P. Jorgensen, J. Bonde, J.H. Nielsen, S. Hørch, I. Chorkendorff, Identification of active edge sites for electrochemical H₂ evolution from MoS₂ nanocatalysts, *Science* 317 (2007) 100–102.
- D. Voiry, H. Yamaguchi, J.W. Li, R. Silva, D.C.B. Alves, T. Fujita, M.W. Chen, T. Asefa, V.B. Shenoy, G. Edda, M. Chhowalla, Enhanced catalytic activity in strained chemically exfoliated WS₂ nanosheets for hydrogen evolution, *Nat. Mater.* 12 (2013) 850–855.
- K. Chang, Z.W. Mei, T. Wang, Q. Kang, S.X. Ouyang, J.H. Ye, MoS₂/graphene cocatalyst for efficient photocatalytic H₂ evolution under visible light irradiation, *ACS Nano* 8 (2014) 7078–7087.
- K. Chang, M. Li, T. Wang, S.X. Ouyang, P. Li, L.Q. Liu, J.H. Ye, Drastic layer-number-dependent activity enhancement in photocatalytic H₂ evolution over nMoS₂/CdS (*n* ≥ 1) under visible light, *Adv. Energy Mater.* 5 (2015) 1402279.
- M.A. Lukowski, A.S. Daniel, F. Meng, A. Forticaux, L.S. Li, S. Jin, Enhanced hydrogen evolution catalysis from chemically exfoliated metallic MoS₂ nanosheets, *J. Am. Chem. Soc.* 135 (2013) 10274–10277.
- J. Kibsgaard, Z.B. Chen, B.N. Reinecke, T.F. Jaramillo, Engineering the surface structure of MoS₂ to preferentially expose active edge sites for electrocatalysis, *Nat. Mater.* 11 (2012) 963–969.
- B. Hinnemann, P.G. Moses, J. Bonde, K.P. Jorgensen, J.H. Nielsen, S. Hørch, I. Chorkendorff, J.K. Nørskov, Biomimetic hydrogen evolution: MoS₂ nanoparticles as catalyst for hydrogen evolution, *J. Am. Chem. Soc.* 127 (2005) 5308–5309.
- H. Li, C. Tsai, A.L. Koh, L.L. Cai, A.W. Contryman, A.H. Fragapane, J.H. Zhao, H.S. Han, H.C. Manoharan, F. Abild-Pedersen, J.K. Nørskov, X.L. Zheng, Activating and optimizing MoS₂ basal planes for hydrogen evolution through the formation of strained sulphur vacancies, *Nat. Mater.* 15 (2016) 48–53.
- P.D. Tran, T.V. Tran, M. Orio, S. Torelli, Q.D. Truong, K. Nayuki, Y. Sasaki, S.Y. Chiam, R. Yi, I. Honma, Coordination polymer structure and revisited hydrogen evolution catalytic mechanism for amorphous molybdenum sulfide, *Nat. Mater.* 15 (2016) 640–646.
- J.F. Xie, H. Zhang, S. Li, R.X. Wang, X. Sun, M. Zhou, J.F. Zhou, X.W. Lou, Y. Xie, Defect-rich MoS₂ ultrathin nanosheets with additional active edge sites for enhanced electrocatalytic hydrogen evolution, *Adv. Mater.* 25 (2013) 5807–5813.
- T.P. Prasad, E. Diemann, A. Muller, Thermal-decomposition of (NH₄)₂MoO₄S₂, (NH₄)₂MoS₄, (NH₄)₂WO₄S₂ and (NH₄)₂WS₄, *J. Inorg. Nucl. Chem.* 35 (1973) 1895–1904.
- J. Kibsgaard, T.F. Jaramillo, F. Besenbacher, Building an appropriate active-site motif into a hydrogen-evolution catalyst with thiomolybdate [Mo₃S₁₃]^{2−} clusters, *Nat. Chem.* 6 (2014) 248–253.
- J. Kibsgaard, Z. Chen, B.N. Reinecke, T.F. Jaramillo, Engineering the surface structure of MoS₂ to preferentially expose active edge sites for electrocatalysis, *Nat. Mater.* 11 (2012) 963–969.
- L. Benoist, D. Gonbeau, G. Pfister-Guilouzo, E. Schmidt, G. Meunier, A. Levasseur, X-ray photoelectron spectroscopy characterization of amorphous molybdenum oxysulfide thin films, *Thin Solid Films* 258 (1995) 110–114.
- L. Oakes, R. Carter, T. Hanken, A.P. Cohn, K. Share, B. Schmidt, C.L. Pint, Interface strain in vertically stacked two-dimensional heterostructured carbon-MoS₂ nanosheets controls electrochemical reactivity, *Nat. Commun.* 7 (2016) 11796.
- H. Wang, P. Skeldon, G. Thompson, XPS studies of MoS₂ formation from ammonium tetrathiomolybdate solutions, *Surf. Coat. Technol.* 91 (1997) 200–207.
- S. Yu, Z.J. Li, X.B. Fan, J.X. Li, F. Zhan, X.B. Li, Y. Tao, C.H. Tung, L.Z. Wu, Vectorial electron transfer for improved hydrogen evolution by mercaptopropionic-acid-regulated CdSe quantum-dots-TiO₂-Ni(OH)₂ assembly, *ChemSusChem* 8 (2015) 642–649.
- Y. He, H.T. Lu, L.M. Sai, Y.Y. Su, M. Hu, C.H. Fan, W. Huang, L.H. Wang, Microwave synthesis of water-dispersed CdTe/CdS/ZnS core-shell-shell quantum dots with excellent photostability and biocompatibility, *Adv. Mater.* 20 (2008) 3416–3421.
- L.R.L. Ting, Y. Deng, L. Ma, Y.-J. Zhang, A.A. Peterson, B.S. Yeo, Catalytic activities of sulfur atoms in amorphous molybdenum sulfide for the electrochemical hydrogen evolution reaction, *ACS Catal.* 6 (2016) 861–867.
- D. Kong, H. Wang, J.J. Cha, M. Pasta, K.J. Koski, J. Yao, Y. Cui, Synthesis of MoS₂ and MoSe₂ films with vertically aligned layers, *Nano Lett.* 13 (2013) 1341–1347.
- X. Huang, M. Leng, W. Xiao, M. Li, J. Ding, T.L. Tan, W.S.V. Lee, J. Xue, Activating basal planes and S-terminated edges of MoS₂ toward more efficient hydrogen evolution, *Adv. Funct. Mater.* 27 (2016) 1604943.
- G. Li, D. Zhang, Q. Qiao, Y. Yu, D. Peterson, A. Zafar, R. Kumar, S. Curtarolo, F. Hunte, S. Shannon, All the catalytic active sites of MoS₂ for hydrogen evolution, *J. Am. Chem. Soc.* 138 (2016) 16632–16638.
- D.R. Cummins, U. Martinez, A. Sherehiy, R. Kappera, A. Martinez-Garcia, R.K. Schulze, J. Jasinski, J. Zhang, R.K. Gupta, J. Lou, Efficient hydrogen evolution in transition metal dichalcogenides via a simple one-step hydrazine reaction, *Nat. Commun.* 7 (2016) 11857.
- K. Maeda, Z-Scheme water splitting using two different semiconductor photocatalysts, *ACS Catal.* 3 (2013) 1486–1503.
- G.J. Guan, S.Y. Zhang, S.H. Liu, Y.Q. Cai, M. Low, C.P. Teng, I.Y. Phang, Y. Cheng, K.L. Duei, B.M. Srinivasan, Y.G. Zheng, Y.W. Zhang, M.Y. Han, Protein induces layer-by-layer exfoliation of transition metal dichalcogenides, *J. Am. Chem. Soc.* 137 (2015) 6152–6155.
- K.F. Mak, C. Lee, J. Hone, J. Shan, T.F. Heinz, Atomically thin MoS₂: a new direct-gap semiconductor, *Phys. Rev. Lett.* 105 (2010) 136805.
- T. Thurston, J. Wilcoxon, Photooxidation of organic chemicals catalyzed by nanoscale MoS₂, *J. Phys. Chem. B* 103 (1999) 11–17.
- T. Rajh, A.E. Ostafin, O.I. Micic, D.M. Tiede, M.C. Thurnauer, Surface modification of small particle TiO₂ colloids with cysteine for enhanced photochemical reduction: an EPR study, *J. Phys. Chem.* 100 (1996) 4538–4545.
- Q. Xiang, J. Yu, M. Jaroniec, Synergistic effect of MoS₂ and graphene as cocatalysts for enhanced photocatalytic H₂ production activity of TiO₂ nanoparticles, *J. Am. Chem. Soc.* 134 (2012) 6575–6578.
- Y.-J. Yuan, Z.-J. Ye, H.-W. Lu, B. Hu, Y.-H. Li, D.-Q. Chen, J.-S. Zhong, Z.-T. Yu, Z.-G. Zou, Constructing anatase TiO₂ nanosheets with exposed (001) facets/layered MoS₂ two-dimensional nanojunctions for enhanced solar hydrogen generation, *ACS Catal.* 6 (2015) 532–541.
- X. Hai, K. Chang, H. Pang, M. Li, P. Li, H. Liu, L. Shi, J. Ye, Engineering the edges of MoS₂ (WS₂) crystals for direct exfoliation into monolayers in polar micromolecular solvents, *J. Am. Chem. Soc.* 138 (2016) 14962–14969.
- J. Chen, X.J. Wu, L. Yin, B. Li, X. Hong, Z. Fan, B. Chen, C. Xue, H. Zhang, One-pot synthesis of CdS nanocrystals hybridized with single-layer transition-metal dichalcogenide nanosheets for efficient photocatalytic hydrogen evolution, *Angew. Chem. Int. Ed.* 54 (2015) 1210–1214.
- Y. Tan, P. Liu, L. Chen, W. Cong, Y. Ito, J. Han, X. Guo, Z. Tang, T. Fujita, A. Hirata, Monolayer MoS₂ films supported by 3D nanoporous metals for high-efficiency electrocatalytic hydrogen production, *Adv. Mater.* 26 (2014) 8023–8028.
- K. Chang, X. Hai, H. Pang, H. Zhang, L. Shi, G. Liu, H. Liu, G. Zhao, M. Li, J. Ye, Targeted synthesis of 2H- and 1T-phase MoS₂ monolayers for catalytic hydrogen evolution, *Adv. Mater.* 28 (2016) 10033–10041.
- Y. Yin, J.C. Han, Y.M. Zhang, X.H. Zhang, P. Xu, Q. Yuan, L. Samad, X.J. Wang, Y. Wang, Z.H. Zhang, P. Zhang, X.Z. Cao, B. Song, S. Jin, Contributions of phase, sulfur vacancies, and edges to the hydrogen evolution reaction catalytic activity of porous molybdenum disulfide nanosheets, *J. Am. Chem. Soc.* 138 (2016) 7965–7972.
- Y. Bensimon, P. Beloune, B. Deroide, J.C. Giuntini, J.V. Zanchetta, Electrical-conductivity in amorphous molybdenum sulfides, *J. Phys. Chem. Solids* 52 (1991) 471–477.